Bianisotropic Metasurfaces for Optimal Polarization Control: Analysis and Synthesis

Carl Pfeiffer and Anthony Grbic*

Department of Electrical Engineering and Computer Science, University of Michigan, Ann Arbor, Michigan 48109-2122, USA

(Received 2 May 2014; revised manuscript received 16 July 2014; published 23 October 2014)

Methods to analyze and synthesize two-dimensional, bianisotropic metamaterials (metasurfaces) are presented. First, a general bianisotropic metasurface is analyzed by using closed-form expressions that relate the reflection and transmission coefficients to its constituent surface parameters. Next, a systematic method to synthesize bianisotropic metasurfaces is outlined. It is analytically shown that bianisotropic metasurfaces can be realized by cascading anisotropic, patterned metallic sheets (electric sheet admittances). This geometry allows for straightforward design and fabrication from microwave to optical wavelengths. To demonstrate the utility of the proposed method, four devices exhibiting exotic polarization transformations are presented: a polarization rotator, an asymmetric circular polarizer, an asymmetric linear polarizer, and a symmetric circular polarizer. The optimal performance at centimeter, millimeter, and micrometer wavelengths highlights the versatility of the design process.

DOI: 10.1103/PhysRevApplied.2.044011

I. INTRODUCTION

Metasurfaces that exhibit a purely electric response provide extraordinary capabilities in controlling electromagnetic wave fronts [1–3]. Some of the most exciting examples are subwavelength focusing and the generalization of Snell's laws of refraction [4,5]. Recently, it was shown that adding a magnetic response to metasurfaces can remove reflection losses and dramatically increase their efficiency [6–8]. Here, anisotropy and magnetoelectric coupling are also systematically incorporated into metasurface design to allow for complete control of an electromagnetic wave front's polarization and phase. To date, many structures are reported that exhibit novel polarization effects such as asymmetric transmission [9–12] and giant optical activity [13,14]. However, the performance of most devices is suboptimal, since systematic design methodologies for realizing these low-symmetry structures are limited [13]. Designs typically employ a resonant geometry that exhibits the necessary mirror and rotational symmetry such that a desired bianisotropic response is observed rather than attempting to provide optimal performance [15]. Additionally, the principle of operation is often device specific, and its generalization to other designs is not straightforward.

Previously reported analyses model bianisotropic metasurfaces as coupled electric and magnetic dipoles [16]. In Ref. [13], the interaction of neighboring particles is also considered. However, the model is rather complex, since the polarizabilities relate the induced dipole moment to the incident field rather than the average field [13]. Alternatively, it is possible to model a metasurface as a thin bianisotropic slab [17]. However, the scattering parameters cannot be solved for in closed form unless some simplifying approximations are made [18]. Furthermore, the interpretation is not strictly appropriate, since the thickness of a metasurface is ill defined [19].

Here, methods to both analyze and design bianisotropic metasurfaces are presented. First, bianisotropic metasurfaces are analyzed by using closed-form expressions that relate the reflection and transmission coefficients (scattering parameters) to constituent surface parameters. This method is an alternative approach to that used in Ref. [13] and provides additional physical intuition. Here, the constituent surface parameters relate the induced dipole moments to the average field quantities as in standard homogenization techniques for bulk materials. Next, a method to systematically design bianisotropic structures is introduced. It is shown that cascading anisotropic, patterned metallic sheets can provide significant control over the constituent surface parameters. A transfer-matrix approach is used to directly solve for the scattering parameters (S parameters) of the structure, enabling devices with optimal performance: polarization purity and high transmission. It should be emphasized that the main claim is that the performance, rather than the implementation, is optimal. Finally, the ability to realize a wide range of constituent surface parameters is demonstrated with four different devices: a polarization rotator, an asymmetric circular polarizer, an asymmetric linear polarizer, and a symmetric circular polarizer.

II. ANALYSIS: RELATING S PARAMETERS TO CONSTITUENT SURFACE PARAMETERS

Let us consider two regions of space (regions 1 and 2) with wave impedances given by $\eta_1 = \sqrt{\mu_1/\epsilon_1}$ and

*To whom correspondence should be addressed. agrbic@umich.edu

$\eta_2 = \sqrt{\mu_2/\epsilon_2}$, respectively. The two regions of space are separated by an arbitrary metasurface along the $z = 0$ plane, as shown in Fig. 1. The metasurface is illuminated by a normally incident plane. The scattering parameters (S parameters) are equal to the ratio of the scattered electric field to the incident electric field. In general,

$$\mathbf{S}_{nm} = \begin{pmatrix} S_{nm}^{xx} & S_{nm}^{xy} \\ S_{nm}^{yx} & S_{nm}^{yy} \end{pmatrix}$$

is a 2×2 matrix relating the field scattered into region n when a plane wave is normally incident from region m. For example, S_{21}^{yx} represents the y-polarized field transmitted into region 2 when an x-polarized plane wave is incident from region 1. The parameters $\mathbf{S}_{11}$ and $\mathbf{S}_{22}$ are the reflection coefficients when viewed from regions 1 and 2, respectively, and $\mathbf{S}_{21}$ and $\mathbf{S}_{12}$ are the transmission coefficients when viewed from regions 1 and 2, respectively. The transmission coefficient is often referred to as the Jones matrix [15].

An arbitrary metasurface can be modeled as a two-dimensional array of polarizable particles [20]. Each particle is characterized by its quasistatic electric and magnetic polarizabilities ($\boldsymbol{\alpha}_{e,m}$), defined as the ratio of the dipole moment to the local field. When these particles are closely spaced across a two-dimensional surface, a surface polarizability ($\boldsymbol{\alpha}_{e,m}^{s}$) that accounts for coupling between particles can be defined [20]. They represent the effective polarizability per unit area:

$$\begin{pmatrix} \mathbf{p}^s \\ \mathbf{m}^s \end{pmatrix} = \begin{pmatrix} \boldsymbol{\alpha}_{ee}^s & \boldsymbol{\alpha}_{em}^s \\ \boldsymbol{\alpha}_{me}^s & \boldsymbol{\alpha}_{mm}^s \end{pmatrix} \begin{pmatrix} \mathbf{E} \\ \mathbf{H} \end{pmatrix}. \tag{1}$$

Here, $\mathbf{p}^s = [\, p_x^s \quad p_y^s \,]^T$ and $\mathbf{m}^s = [\, m_x^s \quad m_y^s \,]^T$ represent the electric and magnetic dipole moments, respectively, while $\mathbf{E} = [\, E_x \quad E_y \,]^T$ and $\mathbf{H} = [\, H_x \quad H_y \,]^T$ represent the average field tangential to the surface.

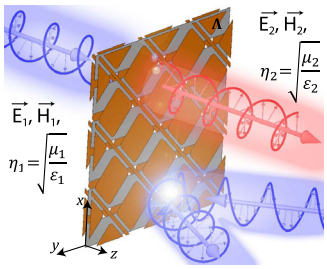

FIG. 1. Metasurfaces exhibiting electric, magnetic, and magnetoelectric responses can achieve complete control of the polarization of an electromagnetic wave front. This artistic rendering shows the example of an asymmetric circular polarizer converting right-handed-circularly-polarized light from region 1 to left-handed-circularly-polarized light in region 2. However, right-handed-circularly-polarized light is completely reflected when incident from region 2.

A time-harmonic progression of $e^{j\omega t}$ is assumed, where ω is the radial frequency and t is time. We then define an electric sheet admittance tensor ($\mathbf{Y} = j\omega\boldsymbol{\alpha}_{ee}^s$), magnetic sheet impedance tensor ($\mathbf{Z} = j\omega\boldsymbol{\alpha}_{mm}^s$), and dimensionless magnetoelectric coupling tensors ($\boldsymbol{\chi} = j\omega\boldsymbol{\alpha}_{em}^s$ and $\Upsilon = j\omega\boldsymbol{\alpha}_{me}^s$ in terms of the surface polarizabilities. By multiplying both sides of Eq. (1) by $j\omega$ and noting that a time-varying dipole moment can be equated to a surface current, the electric and magnetic surface currents established on the metasurface can be related to the average, tangential electric and magnetic fields:

$$\begin{pmatrix} \mathbf{J}^s \\ \mathbf{M}^s \end{pmatrix} = \begin{pmatrix} \mathbf{Y} & \boldsymbol{\chi} \\ \Upsilon & \mathbf{Z} \end{pmatrix} \begin{pmatrix} \mathbf{E} \\ \mathbf{H} \end{pmatrix} = \Lambda \begin{pmatrix} \mathbf{E} \\ \mathbf{H} \end{pmatrix}. \tag{2}$$

The variables $\mathbf{Y}$, $\boldsymbol{\chi}$, Υ, and $\mathbf{Z}$ are all 2×2 tensors that relate the x and y field components to the x and y current-density components:

$$\mathbf{Y} = \begin{pmatrix} Y_{xx} & Y_{xy} \\ Y_{yx} & Y_{yy} \end{pmatrix}, \quad \boldsymbol{\chi} = \begin{pmatrix} \chi_{xx} & \chi_{xy} \\ \chi_{yx} & \chi_{yy} \end{pmatrix},$$
$$\Upsilon = \begin{pmatrix} \Upsilon_{xx} & \Upsilon_{xy} \\ \Upsilon_{yx} & \Upsilon_{yy} \end{pmatrix}, \quad \mathbf{Z} = \begin{pmatrix} Z_{xx} & Z_{xy} \\ Z_{yx} & Z_{yy} \end{pmatrix}.$$

Intuitively, $\mathbf{Y}$ and $\mathbf{Z}$ are the two-dimensional equivalent of electric and magnetic material susceptibilities, respectively [21]. Similarly, $\boldsymbol{\chi}$ and Υ are the two-dimensional equivalent of the magnetoelectric material parameters. If the metasurface is reciprocal, $\mathbf{Y} = \mathbf{Y}^T$, $\Upsilon = -\boldsymbol{\chi}^T$, and $\mathbf{Z} = \mathbf{Z}^T$ [22]. In addition, if it is lossless, $\mathbf{Y}$ and $\mathbf{Z}$ are purely imaginary, whereas Υ and $\boldsymbol{\chi}$ are purely real [22].

The S parameters for normally incident waves can be found by enforcing the boundary condition given by Eq. (2) (see Supplemental Material [23]):

$$\begin{pmatrix} \mathbf{S}_{11} & \mathbf{S}_{12} \\ \mathbf{S}_{21} & \mathbf{S}_{22} \end{pmatrix} = \begin{pmatrix} \frac{\mathbf{Y}}{2} - \frac{\boldsymbol{\chi}\mathbf{n}}{2\eta_1} + \frac{\mathbf{I}}{\eta_1} & \frac{\mathbf{Y}}{2} + \frac{\boldsymbol{\chi}\mathbf{n}}{2\eta_2} + \frac{\mathbf{I}}{\eta_2} \\ -\frac{\mathbf{Z}\mathbf{n}}{2\eta_1} + \frac{\Upsilon}{2} - \mathbf{n} & \frac{\mathbf{Z}\mathbf{n}}{2\eta_2} + \frac{\Upsilon}{2} + \mathbf{n} \end{pmatrix}^{-1}$$
$$\times \begin{pmatrix} -\frac{\mathbf{Y}}{2} - \frac{\boldsymbol{\chi}\mathbf{n}}{2\eta_1} + \frac{\mathbf{I}}{\eta_1} & -\frac{\mathbf{Y}}{2} + \frac{\boldsymbol{\chi}\mathbf{n}}{2\eta_2} + \frac{\mathbf{I}}{\eta_2} \\ -\frac{\mathbf{Z}\mathbf{n}}{2\eta_1} - \frac{\Upsilon}{2} + \mathbf{n} & \frac{\mathbf{Z}\mathbf{n}}{2\eta_2} - \frac{\Upsilon}{2} - \mathbf{n} \end{pmatrix}, \tag{3}$$

where

$$\mathbf{I} = \begin{pmatrix} 1 & 0 \\ 0 & 1 \end{pmatrix}$$

is the identity matrix and

$$\mathbf{n} = \begin{pmatrix} 0 & -1 \\ 1 & 0 \end{pmatrix}$$

is the 90° rotation matrix.

Alternatively, the constituent surface parameters (Λ) can be written in terms of the S parameters (see Supplemental Material [23]), which allows the synthesis of metasurfaces from desired S parameters:

$$\begin{pmatrix} \mathbf{Y} & \boldsymbol{\chi} \\ \boldsymbol{\Upsilon} & \mathbf{Z} \end{pmatrix} = 2\begin{pmatrix} \frac{\mathbf{I}}{\eta_1} - \frac{\mathbf{S}_{11}}{\eta_1} - \frac{\mathbf{S}_{21}}{\eta_2} & \frac{\mathbf{I}}{\eta_2} - \frac{\mathbf{S}_{12}}{\eta_1} - \frac{\mathbf{S}_{22}}{\eta_2} \\ \mathbf{n} + \mathbf{n}\mathbf{S}_{11} - \mathbf{n}\mathbf{S}_{21} & -\mathbf{n} + \mathbf{n}\mathbf{S}_{12} - \mathbf{n}\mathbf{S}_{22} \end{pmatrix} \times \begin{pmatrix} \mathbf{I} + \mathbf{S}_{11} + \mathbf{S}_{21} & \mathbf{I} + \mathbf{S}_{12} + \mathbf{S}_{22} \\ \frac{\mathbf{n}}{\eta_1} - \frac{\mathbf{n}\mathbf{S}_{11}}{\eta_1} + \frac{\mathbf{n}\mathbf{S}_{21}}{\eta_2} & -\frac{\mathbf{n}}{\eta_2} - \frac{\mathbf{n}\mathbf{S}_{12}}{\eta_1} + \frac{\mathbf{n}\mathbf{S}_{22}}{\eta_2} \end{pmatrix}^{-1}. \tag{4}$$

Similar to material parameter extraction procedures for bulk metamaterials [24], Eqs. (3) and (4) provide a powerful framework to design and analyze metasurfaces that realize arbitrary polarization, phase, and amplitude transformations. It is also interesting to note that these expressions are virtually identical to those derived in Ref. [18] for a thin bianisotropic material slab. However, it has been shown that it is generally more appropriate to treat metasurfaces as boundary conditions supporting electric and magnetic surface currents as is done here [19].

III. SYNTHESIS

A. Relating S parameters to cascaded sheet admittances

Next, a geometry is proposed that can achieve a wide range of constituent surface parameters. The geometry consists of cascaded metallic sheets (electric sheet admittances) separated by subwavelength dielectric spacers, as shown in Fig. 2. It should be emphasized that this cascaded structure can be modeled by using the constitutive surface parameters derived in the previous section, provided that its overall thickness is subwavelength. This geometry is attractive, because it allows for straightforward design and fabrication from microwave to optical wavelengths [25–29]. Inspiration for this geometry is derived from recent work showing that the diagonal elements of the electric and magnetic surface susceptibility tensors can be completely controlled with cascaded sheets [8]. Recent work has also shown that polarization-controlling devices, such as quarter-wave plates, half-wave plates, and circular polarizers, can be realized by cascading anisotropic sheets [29–32].

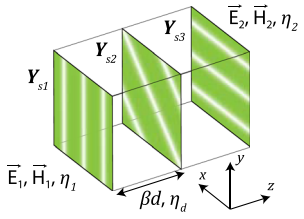

FIG. 2. Anisotropic sheet admittances cascaded in the direction of propagation can realize a wide range of constituent surface parameters. Provided the overall thickness of the cascaded sheets is subwavelength, they can be modeled as a single bianisotropic metasurface.

A transfer-matrix (**ABCD**-matrix) approach is employed to develop a relation between the cascaded sheet admittances and the S parameters [32]. This approach relates the total field in regions 1 and 2 by the **ABCD** matrix:

$$\begin{pmatrix} \mathbf{E}_1 \\ \mathbf{H}_1 \end{pmatrix} = \begin{pmatrix} \mathbf{A} & \mathbf{B} \\ \mathbf{C} & \mathbf{D} \end{pmatrix} \begin{pmatrix} \mathbf{E}_2 \\ \mathbf{H}_2 \end{pmatrix}, \tag{5}$$

where **A**, **B**, **C**, and **D** are each 2×2 matrices relating the x and y field components. For example, three cascaded sheet admittances have the transfer matrix

$$\begin{aligned} &\begin{pmatrix} \mathbf{A} & \mathbf{B} \\ \mathbf{C} & \mathbf{D} \end{pmatrix} \\ &= \left[\begin{pmatrix} \mathbf{I} & \mathbf{0} \\ \mathbf{n}\mathbf{Y}_{s1} & \mathbf{I} \end{pmatrix} \begin{pmatrix} \cos(\beta d)\mathbf{I} & -j\sin(\beta d)\eta_d \mathbf{n} \\ j\sin(\beta d)\eta_d^{-1}\mathbf{n} & \cos(\beta d)\mathbf{I} \end{pmatrix} \right. \\ &\quad \times \begin{pmatrix} \mathbf{I} & \mathbf{0} \\ \mathbf{n}\mathbf{Y}_{s2} & \mathbf{I} \end{pmatrix} \begin{pmatrix} \cos(\beta d)\mathbf{I} & -j\sin(\beta d)\eta_d \mathbf{n} \\ j\sin(\beta d)\eta_d^{-1}\mathbf{n} & \cos(\beta d)\mathbf{I} \end{pmatrix} \\ &\quad \left. \times \begin{pmatrix} \mathbf{I} & \mathbf{0} \\ \mathbf{n}\mathbf{Y}_{s3} & \mathbf{I} \end{pmatrix} \right]. \end{aligned} \tag{6}$$

Here, η_d is the substrate impedance (impedance of the dielectric spacers), βd is the interlayer electrical spacing, and $\mathbf{Y}_{sn}$ is the admittance of the nth sheet (see Fig. 2).

The reflection and transmission coefficients of the structure can then be related to the **ABCD** matrix of the cascaded sheet admittances (see Supplemental Material [23]):

$$\begin{pmatrix} \mathbf{S}_{11} & \mathbf{S}_{12} \\ \mathbf{S}_{21} & \mathbf{S}_{22} \end{pmatrix} = \begin{pmatrix} -\mathbf{I} & \frac{\mathbf{B}\mathbf{n}}{\eta_2} + \mathbf{A} \\ \frac{\mathbf{n}}{\eta_1} & \frac{\mathbf{D}\mathbf{n}}{\eta_2} + \mathbf{C} \end{pmatrix}^{-1} \begin{pmatrix} \mathbf{I} & \frac{\mathbf{B}\mathbf{n}}{\eta_2} - \mathbf{A} \\ \frac{\mathbf{n}}{\eta_1} & \frac{\mathbf{D}\mathbf{n}}{\eta_2} - \mathbf{C} \end{pmatrix}. \tag{7}$$

Now that a relation between cascaded sheet admittances and the S parameters is established, the sheets can be systematically designed to achieve desired S parameters.

B. Finding and realizing the sheet admittances

Analytically solving for the S parameters of a given structure is straightforward. For example, the S parameters of three cascaded sheet admittances can be found by inserting Eq. (6) into Eq. (7). However, we are looking to solve the inverse problem: stipulating the S parameters and solving for the necessary sheet admittances. Since the necessary sheet admittances have not been solved analytically, a numerical solver is employed. The *fmincon* function provided by MATLAB's optimization toolbox is used to perform a gradient-descent method. The specific cost function that is minimized is $|S_{21}^{xx} - T^{xx}|^2 + |S_{21}^{xy} - T^{xy}|^2 + |S_{21}^{yx} - T^{yx}|^2 + |S_{21}^{yy} - T^{yy}|^2$, where $\mathbf{S}_{21}$ is the transmission

coefficient of the cascaded sheet admittances and **T** is the desired transmission coefficient. Since this is a nonlinear problem, the gradient-descent method may return only a local minimum rather than the global minimum, depending on the initial starting point. Nevertheless, the optimizer typically converges to the global minimum with less than ten randomly seeded initial starting points.

Once the required sheet admittances are known, their physical realization is straightforward by using frequency-selective surface theory [33,34]. Typically, each sheet consists of patterned metal on a dielectric substrate. At optical frequencies, dielectric patterning also becomes an attractive option [8,35]. Here, the metallic pattern is designed through scattering simulations using the full-wave solver ANSYS HFSS. Figure 3 demonstrates how each sheet is simulated. Floquet ports excite normally incident plane waves, which are deembedded to the pattered sheet located at the $z = 0$ plane. Infinite periodicity is assumed by stipulating periodic boundary conditions along the other four sides. As shown in Fig. 3, the sheet admittance is generally located between two different media with wave impedances given by η_1 and η_2. It is important to note that, in addition to the metallic pattern, the sheet admittance itself is also a function of the surrounding dielectric media.

An iterative approach is used to design the sheet admittance. First, the dimensions of a metallic pattern are stipulated, and the structure is simulated. The sheet admittance is extracted from simulation by noting the simulated reflection coefficients:

$$\begin{aligned}\mathbf{Y}_s &= \left(\frac{\mathbf{I}-\mathbf{S}_{11}}{\eta_1}-\frac{\mathbf{I}+\mathbf{S}_{11}}{\eta_2}\right)(\mathbf{I}+\mathbf{S}_{11})^{-1} \\ &= \left(\frac{\mathbf{I}-\mathbf{S}_{22}}{\eta_2}-\frac{\mathbf{I}+\mathbf{S}_{22}}{\eta_1}\right)(\mathbf{I}+\mathbf{S}_{22})^{-1}. \qquad (8)\end{aligned}$$

Then, by considering the equivalent circuit of the sheet, the dimensions are adjusted while also attempting to maximize bandwidth and minimize loss. Once the sheet admittances are realized, their cascaded response is calculated by using the transfer-matrix approach described earlier. It should be noted that the transfer-matrix approach accounts for only propagating modes within the structure, and evanescent modes are neglected. Thus, the analysis works only when evanescent coupling between the sheets is low. The accuracy of this approximation is improved by reducing the cell size and increasing the interlayer spacing.

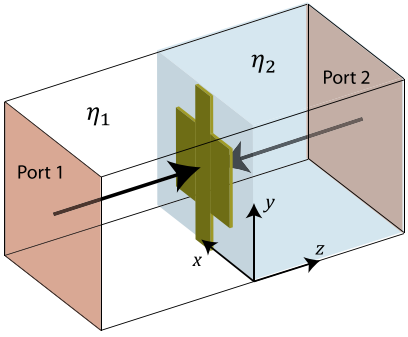

FIG. 3. Simulation used to design each sheet admittance.

IV. BIANISOTROPIC METASURFACE EXAMPLES

To demonstrate the versatility of the design process, four devices exhibiting novel polarization transformations are presented: a polarization rotator, an asymmetric circular polarizer, an asymmetric linear polarizer, and a symmetric circular polarizer. Each structure requires significantly different constituent surface parameters. For additional details on the measurement procedures, exact dimensions, simulations, and analyses, please refer to the Supplemental Material [23].

It should be emphasized that the reported structures operate fundamentally differently from devices that achieve polarization control through cascading Jones matrices. The structures reported here rely on the interference of multiple reflections between the sheets to achieve various phase discontinuities and novel polarization effects while also maintaining a subwavelength profile. In contrast, simply cascading the Jones matrices of wave plates and linear polarizers does not take advantage of the multiple reflections between sheets, and therefore the resulting devices are significantly bulkier [36].

A. Polarization rotator at microwave frequencies

Chiral materials with a strong rotary power are commonly used in analytical chemistry, biology, and crystallography for identifying the spatial structure of molecules [37]. Chirality can also provide an alternative route to achieve negative refraction [38]. A particularly interesting structure that exhibits a strong chiral response is the polarization rotator, which rotates an incident linear polarization by 90° upon transmission. Previously, polarization rotation was accomplished with an isotropic helical structure [13]. However, the three-dimensional geometry requires metallized via holes, which become prohibitively difficult to fabricate at higher frequencies, especially optical frequencies. In addition, the structure exhibits a large insertion loss ($S_{21} = -5$ dB) at the 10 GHz operating frequency. Alternatively, bilayered metamaterials that utilize two sheet admittances (patterned metallic surfaces) separated by an electrically thin dielectric can also act as polarization rotators [14,37]. These works demonstrate that complex helical patterns are not required to achieve significant chirality. In Ref. [37], it is shown that such bilayered metamaterials can have orders-of-magnitude-larger rotary powers than naturally occurring gyrotropic crystals in the visible spectrum. The rotary power is later increased by optimizing the patterns on each sheet [14]. However, the design process is not straightforward, which

leads to a narrow bandwidth and low transmission coefficient (−5 dB) at the operating frequency. Because of the nonoptimal design, the frequencies at which the metasurface achieve peak transmission and 90° polarization rotation are not the same. Here, a systematic method for designing polarization rotators is presented, resulting in optimal performance.

A polarization rotator with a reflection coefficient equal to zero and transmission coefficient equal to

$$\mathbf{S}_{21} = e^{j\phi}\begin{pmatrix} 0 & -1 \\ 1 & 0 \end{pmatrix} \tag{9}$$

is considered [13,14]. In other words, any linearly polarized incident plane wave traveling in the $+z$ direction will undergo a clockwise polarization rotation of 90° upon transmission, when viewed from region 1. By inserting Eq. (9) into Eq. (4), the ideal constituent parameters of such a device are

$$\Lambda = \begin{pmatrix} \frac{-2j\tan(\phi)}{\eta_\circ} & 0 & -2\sec(\phi) & 0 \\ 0 & \frac{-2j\tan(\phi)}{\eta_\circ} & 0 & -2\sec(\phi) \\ 2\sec(\phi) & 0 & -2j\eta_\circ\tan(\phi) & 0 \\ 0 & 2\sec(\phi) & 0 & -2j\eta_\circ\tan(\phi) \end{pmatrix}. \tag{10}$$

The metasurface is isotropic and chiral.

When realizing polarization transformations, the absolute phase delay (ϕ) generated by the metasurface is typically not important for most applications. Therefore, the phase delay can be viewed as a free parameter that can be adjusted to increase the bandwidth and reduce the loss of the metasurface.

The polarization rotator considered here consists of four patterned metallic sheets. The fourth sheet allows added bandwidth. To analyze this structure, Eq. (6) is modified to account for the fourth sheet:

$$\begin{aligned} &\begin{pmatrix} \mathbf{A} & \mathbf{B} \\ \mathbf{C} & \mathbf{D} \end{pmatrix} \\ &= \left[\begin{pmatrix} \mathbf{I} & \mathbf{0} \\ \mathbf{n}\mathbf{Y}_{s1} & \mathbf{I} \end{pmatrix}\begin{pmatrix} \cos(\beta d_1)\mathbf{I} & -j\sin(\beta d_1)\eta_d\mathbf{n} \\ j\sin(\beta d_1)\eta_d^{-1}\mathbf{n} & \cos(\beta d_1)\mathbf{I} \end{pmatrix}\right. \\ &\quad\times\begin{pmatrix} \mathbf{I} & \mathbf{0} \\ \mathbf{n}\mathbf{Y}_{s2} & \mathbf{I} \end{pmatrix}\begin{pmatrix} \cos(\beta d_2)\mathbf{I} & -j\sin(\beta d_2)\eta_d\mathbf{n} \\ j\sin(\beta d_2)\eta_d^{-1}\mathbf{n} & \cos(\beta d_2)\mathbf{I} \end{pmatrix} \\ &\quad\times\begin{pmatrix} \mathbf{I} & \mathbf{0} \\ \mathbf{n}\mathbf{Y}_{s3} & \mathbf{I} \end{pmatrix}\begin{pmatrix} \cos(\beta d_1)\mathbf{I} & -j\sin(\beta d_1)\eta_d\mathbf{n} \\ j\sin(\beta d_1)\eta_d^{-1}\mathbf{n} & \cos(\beta d_1)\mathbf{I} \end{pmatrix} \\ &\quad\left.\times\begin{pmatrix} \mathbf{I} & \mathbf{0} \\ \mathbf{n}\mathbf{Y}_{s4} & \mathbf{I} \end{pmatrix}\right]. \end{aligned} \tag{11}$$

It should be noted that, due to the adhesive layers used in fabrication, the middle dielectric spacer (d_2) is a different thickness than the outer dielectric spacers (d_1).

The necessary cascaded sheet admittances that realize a polarization rotator are numerically found by inserting Eq. (9) into Eq. (7) and combining the result with Eq. (11). If the operating frequency equals 10 GHz, $\phi = -40°$, $\eta_1 = \eta_2 = \eta_\circ$, $\eta_d = \eta_\circ/1.88$, $\beta d_1 = 2\pi/10.48$, and $\beta d_2 = 2\pi/9.54$, the required sheet admittances are

$$\mathbf{Y}_{s1} = \frac{j}{\eta_\circ}\begin{pmatrix} 0.92 & -1.39 \\ -1.39 & 2.14 \end{pmatrix},$$
$$\mathbf{Y}_{s2} = \frac{j}{\eta_\circ}\begin{pmatrix} 5.21 & -8.07 \\ -8.07 & 5.21 \end{pmatrix},$$
$$\mathbf{Y}_{s3} = \frac{j}{\eta_\circ}\begin{pmatrix} 7.88 & -1.17 \\ -1.17 & 2.50 \end{pmatrix},$$
$$\mathbf{Y}_{s4} = \frac{j}{\eta_\circ}\begin{pmatrix} 5.67 & 0 \\ 0 & -2.63 \end{pmatrix}.$$

It is found that a transmitted phase of $\phi = -40°$ maximizes the bandwidth.

The bianisotropic metasurface is fabricated by patterning four metallic sheets on 1.52-mm-thick, Rogers 4003 substrates ($\epsilon_r = 3.55$ and $\tan\delta = 0.0027$). A section of the developed polarization rotator is shown in Fig. 4(a), while the bottom sheet of the fabricated structure is shown in Fig. 4(b). The transmission coefficient of the polarization rotator is characterized by illuminating it with a normally incident Gaussian beam and then probing the transmitted field with a near-field scanning system [23,39–41]. The simulated and measured performance is shown in Fig. 4(c). There is a 2% frequency shift between the measurement and simulation due to fabrication tolerances. It is also important to note that Eq. (10) dictates that a polarization rotator must be isotropic. The isotropic response of the fabricated structure is verified by rotating the incident linear polarization by an angle θ about the z axis. As shown in Fig. 4(d), the measured cross-polarized (rotated) transmission coefficient is high and independent of the incident linear polarization at the operating frequency of 9.8 GHz. In contrast, the more common half-wave plate achieves high cross-polarization (rotated field) only when the incident field is polarized 45° relative to its crystal axis. The fractional bandwidth of this structure is measured to be 8.7%. The bandwidth is defined as the frequency range over which the cross-polarized transmission coefficient is greater than −3 dB and a copolarized transmission coefficient is less than −10 dB, independent of the incident linear polarization.

It should be noted that the polarization rotator is the only structure presented here that utilizes four patterned sheets. Initially, three sheets were used to realize a polarization rotator. However, the simulated bandwidth was narrow (0.6%) and the loss was high ($S_{21} = -1.7$ dB), which lead to a structure that was extremely sensitive to fabrication tolerances. Therefore, a fourth layer is added to provide

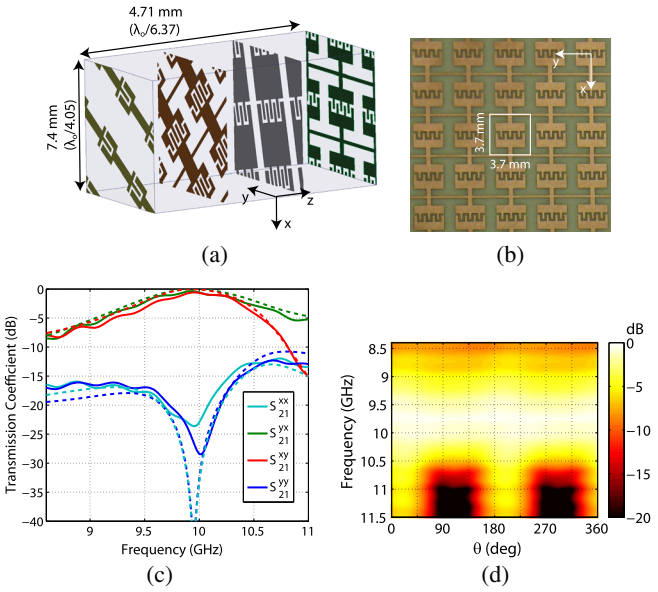

FIG. 4. Metasurface exhibiting polarization rotation near 10 GHz. (a) Schematic of the unit cell. For clarity, the z axis is scaled by a factor of 3 so that all four sheets are visible. (b) Bottom sheet ($\mathbf{Y}_{s4}$) of the fabricated polarization rotator. (c) Transmission coefficient for an incident plane wave traveling in the $+z$ direction. Measured data are denoted by solid lines, whereas simulated are denoted by dashed lines. For clarity, the measured data are frequency shifted by $+0.20$ GHz in the plot. (d) Measured cross-polarized transmission coefficient as a function of frequency and incident linear polarization. The angle θ refers to the angle between the x and y axes of the incident linear polarization. It can be seen that the cross-polarized transmission coefficient is near 0 dB, independent of θ.

additional degrees of freedom that are exploited to increase bandwidth and reduce loss.

B. Asymmetric circular polarizer at millimeter-wave frequencies

Additional control over the constituent surface parameters is demonstrated with a metasurface that provides asymmetric transmission for circularly polarized waves at millimeter-wave frequencies. This effect exhibits some similarity to Faraday rotation but requires no magnetic field or nonreciprocal materials [9]. In addition, this metasurface acts as a circular polarizer, since it transmits circular polarization of one handedness and reflects the other. Demonstrating this effect at millimeter-wave frequencies is particularly useful for a number of reasons. Millimeter wavelengths are long enough to easily propagate through visibly opaque media while short enough to realize large operating bandwidths and millimeter resolution [42]. This property enables high-resolution radar and imaging systems, as well as high-bandwidth communication. In particular, 77 GHz is relevant to automotive radar systems [43].

To date, the most common method to realize asymmetric circular transmission is with a purely electric response: printing two-dimensional chiral patterns on a single sheet [9]. In such a scheme, the asymmetric response is significant only when the eigenvectors of the sheet admittance are complex, which requires high loss. Therefore, the efficiency of these structures is fundamentally limited. The asymmetric response is often defined as the difference between the transmittance of a given handedness of circular polarization, propagating in the $+z$ and $-z$ directions. It is typically low for single sheet geometries (not exceeding 0.25) [10]. Alternatively, it was recently shown that a bilayered metasurface realized by cascading two-dimensional chiral patterns can achieve a larger asymmetric response of 0.6 [10]. However, the design procedure and physical description are vague, and the transmittance and asymmetric response are still too low for most applications. In contrast, the metasurface presented here achieves a near-optimal asymmetric response of 0.99 at the design frequency. In addition, a thorough analysis and systematic design procedure is outlined. This procedure can also be scaled to optical frequencies [29].

The metasurface converts right-handed circular to left-handed circular when traveling in the $+z$ direction. It exhibits the following transmission coefficient:

$$\mathbf{S}_{21} = \frac{e^{j\phi}}{2}\begin{pmatrix} 1 & j \\ j & -1 \end{pmatrix}. \tag{12}$$

However, when propagating in the $-z$ direction, the same metasurface converts left-handed circular to right-handed circular. Therefore, it exhibits asymmetric transmission for circularly polarized waves. It should be noted that this result does not violate reciprocity, since $\mathbf{S}_{21} = \mathbf{S}_{12}^{T}$. Hence, the performance of the structure can be analyzed by considering only plane waves incident from region 1. The constituent surface parameters of the metasurface are given by

$$\Lambda = \begin{pmatrix} \frac{-2j\tan(\phi/2)}{\eta_\circ} & 0 & 0 & 0 \\ 0 & \frac{2j\cot(\phi/2)}{\eta_\circ} & 0 & 0 \\ 0 & 0 & -2j\eta_\circ\tan(\phi) & 2j\eta_\circ\sec(\phi) \\ 0 & 0 & 2j\eta_\circ\sec(\phi) & -2j\eta_\circ\tan(\phi) \end{pmatrix}. \tag{13}$$

As was previously noted, asymmetric transmission does not require three-dimensional chirality ($\boldsymbol{\chi} = \Upsilon = 0$) [9,15]. However, the principal axes of the electric and magnetic responses should be rotated with respect to each other, since $Y_{xy} = 0$ and $Z_{xy} \neq 0$.

The asymmetric circular polarizer has the following properties: $\phi = 175°$, $\beta d = 2\pi/6.37$, $\eta_d = \eta_\circ/1.483$, and $\eta_1 = \eta_2 = \eta_\circ$. The necessary sheet admittances are then numerically solved for

$$\mathbf{Y}_{s1} = \frac{j}{\eta_\circ}\begin{pmatrix} 1.01 & -1.00 \\ -1.00 & 1.01 \end{pmatrix},$$
$$\mathbf{Y}_{s2} = \frac{j}{\eta_\circ}\begin{pmatrix} 2.19 & 0 \\ 0 & -200 \end{pmatrix},$$
$$\mathbf{Y}_{s3} = \frac{j}{\eta_\circ}\begin{pmatrix} 1.01 & -1.00 \\ -1.00 & 1.01 \end{pmatrix}.$$

To realize the sheet admittances, copper is patterned on 380-μm-thick, Rogers 5880 Duroid substrates ($\epsilon_r = 2.2$ and $\tan\delta = 0.0009$. For an operating frequency of 77 GHz, the designed unit cell is shown in Fig. 5(a), while the top sheet of the fabricated structure is shown in Fig. 5(b). The simulated and measured transmission coefficients are shown in Fig. 5(c). The surface exhibits near-perfect conversion of right-handed circular into left-handed circular when propagating in the $+z$ direction. In addition, the measured asymmetric response is broadband: S_{21}^{++}, S_{21}^{+-}, and S_{21}^{--} are below -10 dB, and S_{21}^{-+} is above -0.8 dB, over a bandwidth of 20%. The superscript + denotes right-handed-circular polarization, and − denotes left-handed-circular polarization.

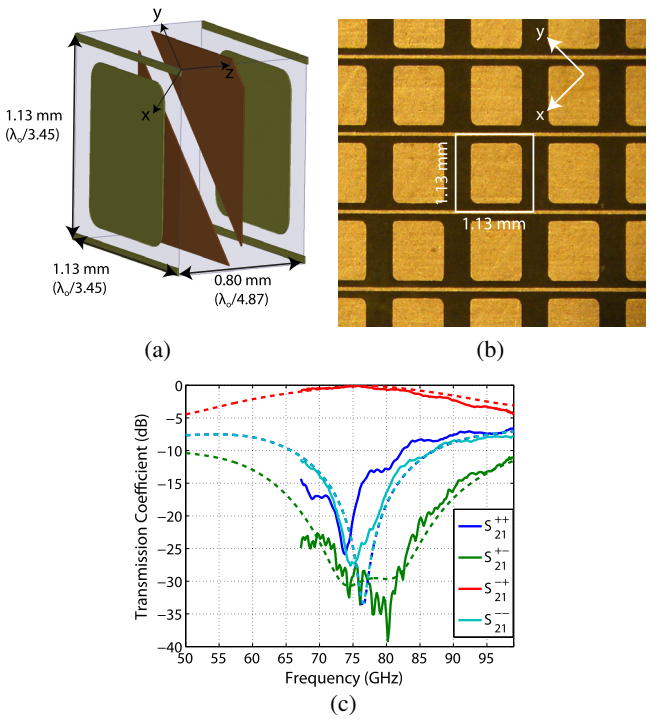

FIG. 5. Metasurface exhibiting asymmetric circular transmission at millimeter-wave frequencies. (a) Schematic of the unit cell. (b) Top sheet ($\mathbf{Y}_{s1}$) of the fabricated asymmetric circular polarizer. (c) Transmission coefficient for an incident plane wave traveling in the $+z$ direction, where the superscript + denotes right-handed circular and − denotes left-handed circular. Measured data are denoted by solid lines, whereas simulated are denoted by dashed lines.

It should be noted that the constituent surface parameters of the ideal asymmetric circular polarizer [Eq. (13)] are a function of the stipulated reflection coefficients in addition to the transmission coefficient. Equation (13) assumes the reflection coefficients are equal to

$$\mathbf{S}_{11} = \mathbf{S}_{22} = \frac{e^{j\phi}}{2}\begin{pmatrix} 1 & -j \\ -j & -1 \end{pmatrix}. \tag{14}$$

In other words, when left-handed circular is incident in the $+z$ direction, all of the power is reflected to left-handed circular [36]. Similarly, when right-handed circular is incident in the $-z$ direction, all of the power is reflected to right-handed circular.

C. Asymmetric linear polarizer at millimeter-wave frequencies

Asymmetric transmission for linearly polarized waves requires geometries that do not exhibit mirror or rotational symmetry [15]. These metasurfaces can be used to increase the polarization diversity of microwave and optical devices. Previously, devices exhibiting asymmetric linear transmission were realized with two- and three-layered chiral meta-atoms [44–46] or asymmetric helical geometries [16]. Although a near-optimal polarization purity is achieved, the response is narrowband [45]. A more straightforward design procedure based on Fabry-Pérot resonances is reported in Ref. [47]. This approach leads to an enhanced bandwidth but at the expense of an increased electrical thickness.

Here, an analytic approach is used to systematically design arbitrarily thin metasurfaces. The asymmetric linear polarizer considered here has the following transmission coefficient:

$$\mathbf{S}_{21} = e^{j\phi}\begin{pmatrix} 0 & 0 \\ 1 & 0 \end{pmatrix}. \tag{15}$$

When an x-polarized plane wave is incident from region 1, it is transmitted as a y-polarized plane wave in region 2. However, if an x-polarized plane wave is incident from region 2, all the power is reflected. Hence, the structure exhibits asymmetric transmission for linear polarization. Assuming the undesired polarization is completely reflected,

$$\mathbf{S}_{11} = e^{j\phi}\begin{pmatrix} 0 & 0 \\ 0 & -1 \end{pmatrix},$$
$$\mathbf{S}_{22} = e^{j\phi}\begin{pmatrix} -1 & 0 \\ 0 & 0 \end{pmatrix}, \tag{16}$$

this metasurface has the constituent surface parameters given by

$$\Lambda = \begin{pmatrix} 4j\eta_\circ^{-1}\cot(\phi) & -4j\eta_\circ^{-1}\csc(\phi) & 0 & -2 \\ -4j\eta_\circ^{-1}\csc(\phi) & 4j\eta_\circ^{-1}\cot(\phi) & -2 & 0 \\ 0 & 2 & 0 & 0 \\ 2 & 0 & 0 & 0 \end{pmatrix}. \quad (17)$$

It can be seen that both an anisotropic electric susceptibility and anisotropic magnetoelectric coupling tensors are required. Again, the necessary sheet admittances are solved by inserting Eqs. (15) and (16) into Eq. (7) and combining the result with Eq. (6). By setting $\phi = 135°$, $\beta d = 2\pi/6.37$, $\eta_d = \eta_\circ/1.483$, and $\eta_1 = \eta_2 = \eta_\circ$, the necessary sheet admittances are

$$\mathbf{Y}_{s1} = \frac{j}{\eta_\circ}\begin{pmatrix} 0.88 & 0 \\ 0 & -77.0 \end{pmatrix},$$
$$\mathbf{Y}_{s2} = \frac{j}{\eta_\circ}\begin{pmatrix} -0.70 & 4.15 \\ 4.15 & -0.70 \end{pmatrix},$$
$$\mathbf{Y}_{s3} = \frac{j}{\eta_\circ}\begin{pmatrix} -77.0 & 0 \\ 0 & 0.88 \end{pmatrix}.$$

A unit cell of this metasurface is shown in Fig. 6(a). The simulated cross-polarized and copolarized transmission coefficients are shown in Fig. 6(b). Although the structure is designed for an operating frequency of 77 GHz, the performance is quite broadband. A 1-dB transmission bandwidth of 2.43:1 for the desired polarization is achieved. The rejection of the unwanted polarization is greater than 30 dB in this band. S_{11}^{yy} is greater than −0.01 dB, and all other S parameters are less than −30 dB over the entire operating bandwidth and are not shown.

D. Symmetric circular polarizer at optical frequencies

As a final demonstration of the versatility of the design process, a symmetric circular polarizer is demonstrated at optical frequencies. Analogous to conventional linear polarizers, these structures transmit one handedness of circular polarization but reflect the other, independent of the propagation direction ($+\hat{z}$ or $-\hat{z}$). At optical frequencies, circular polarizers are attractive for color displays, microscopy, and photography [48]. These devices are most commonly realized by combining quarter-wave plates and linear polarizers [36]. However, this method leads to bulky structures that do not lend themselves to optical integration. Recently, helical structures have demonstrated a reduced thickness and much broader bandwidth [48,49]. However, they require a restrictively difficult fabrication process, which motivates cascading patterned metallic sheets with rotated principal axes [32].

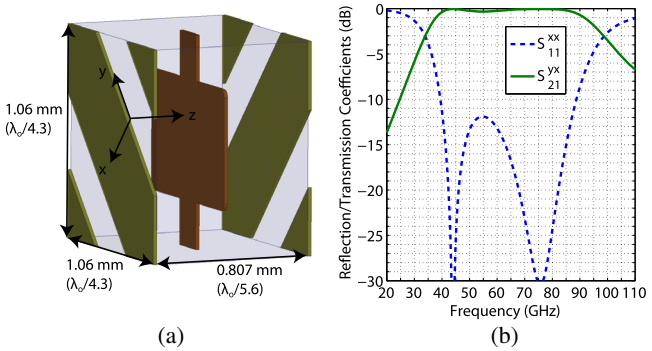

(a) (b)

FIG. 6. Metasurface exhibiting asymmetric linear transmission. (a) Schematic of the unit cell. (b) Simulated copolarized reflection coefficient (S_{11}^{xx}) and cross-polarized transmission coefficient (S_{21}^{yx}) for an incident plane wave traveling in the $+z$ direction. S_{11}^{yy} is greater than −0.01 dB, and all other S parameters are less than −30 dB over the entire frequency range and are not shown.

The symmetric circular polarizer considered here transmits right-handed-circularly-polarized light but reflects the left-handed-circular polarization, regardless of the propagation direction. The transmission coefficient is given by

$$\mathbf{S}_{21} = \frac{e^{j\phi}}{2}\begin{pmatrix} 1 & j \\ -j & 1 \end{pmatrix}, \quad (18)$$

and the constituent surface parameters are given by

$$\Lambda = \begin{pmatrix} \frac{-2j\tan(\phi/2)}{\eta_\circ} & 0 & 0 & 0 \\ 0 & \frac{2j\cot(\phi)}{\eta_\circ} & 0 & -2\csc(\phi) \\ 0 & 0 & -2j\eta_\circ\tan(\phi/2) & 0 \\ 0 & 2\csc(\phi) & 0 & 2j\eta_\circ\cot(\phi) \end{pmatrix}. \quad (19)$$

This metasurface exhibits anisotropic electric and magnetic susceptibilities, as well as magnetoelectric coupling. Equation (19) assumes that both regions 1 and 2 are composed of free space and that the reflection coefficients are given by

$$\mathbf{S}_{11} = \frac{e^{j\phi}}{2}\begin{pmatrix} 1 & -j \\ -j & -1 \end{pmatrix}, \qquad \mathbf{S}_{22} = \frac{e^{j\phi}}{2}\begin{pmatrix} 1 & j \\ j & -1 \end{pmatrix}. \quad (20)$$

In other words, left-handed-circularly-polarized light is completely reflected into left-handed-circular polarization from both the front and the back of the metasurface, whereas right-handed-circularly-polarized light has zero reflection.

Since optical metasurfaces are typically fabricated on a bulk substrate, it is assumed that region 2 is SiO_2 ($n = 1.444$). The dielectric spacer between the sheets is SU-8 ($n = 1.572$), and the permittivity of the Au is described by a Drude model, $\epsilon_{\mathrm{Au}} = \epsilon_\infty - \omega_p^2/(\omega^2 + j\omega\omega_c)$, with $\epsilon_\infty = 9.0$, $\omega_p = 1.363 \times 10^{16}$ rad/s (8.97 eV), and collision frequency $\omega_c = 3.60 \times 10^{14}$ rad/s (0.24 eV). This collision frequency is 3 times greater than that of bulk

Au [50], in order to account for thin-film scattering and grain-boundary effects [51]. This large loss does present some limitations on realizing extreme values of the sheet admittance. Nevertheless, as will be shown, a high performance is still achieved. This structure can be fabricated by sequential patterning of each metallic layer using standard lithography and liftoff processes [27–29,32].

By again looking to Eqs. (6) and (7) and setting $\phi = 170^\circ$, $\beta d = 2\pi/4.77$, $\eta_d = \eta_\circ/1.572$, $\eta_1 = \eta_\circ$, and $\eta_2 = \eta_\circ/1.444$, the necessary sheet admittances to realize a symmetric circular polarizer become

$$\mathbf{Y}_{s1} = \frac{j}{\eta_\circ}\begin{pmatrix} 0.34 & -1.11 \\ -1.11 & 0.34 \end{pmatrix},$$
$$\mathbf{Y}_{s2} = \frac{j}{\eta_\circ}\begin{pmatrix} 1.10 & 0 \\ 0 & -9.00 \end{pmatrix},$$
$$\mathbf{Y}_{s3} = \frac{j}{\eta_\circ}\begin{pmatrix} 0.57 & 1.57 \\ 1.57 & 0.57 \end{pmatrix}.$$

When solving for the cascaded sheet admittances, an upper bound on the maximum value of the sheet admittances is imposed due to limitations in achieving extremely small feature sizes at optical frequencies. The magnitude of the sheets is required to be less than $9.0/\eta_\circ$. The designed unit cell is shown in Fig. 7(a). The simulated transmission coefficient is shown in Fig. 7(b). The superscript + denotes right-handed-circular polarization, and − denotes left-handed-circular polarization. It can be seen that, at the design frequency of 1.5 μm, the metasurface achieves low loss for right-handed-circularly-polarized light and provides greater than 15 dB of rejection for left-handed-circularly-polarized light. For completeness, the transmittance is also plotted on a linear scale in Fig. 7(c), so that its performance can be easily compared to earlier reported structures [32,49].

The performance of this structure exceeds that of previous metasurfaces in a few respects. At the operating frequency, the structure presented here achieves a polarization rejection of 15 dB. This performance is comparable to the rejection levels of the Au helix metamaterial [49], which achieves a larger bandwidth at the expense of significantly increased fabrication complexity and overall thickness. This polarization rejection is also an order of magnitude higher than the previous three-layer structure that cascaded identical electric dipoles with a rotation between the sheets [32].

As with many optical designs, metallic loss reduces the performance compared to the other metasurfaces presented at lower frequencies. To demonstrate that this reduced performance is only a result of high loss at near-infrared frequencies and not a result of the stipulated polarization transformation, a design is also reported at 77 GHz in the Supplemental Material [23]. In addition, it is compared to previously reported structures operating at microwave frequencies [52–56].

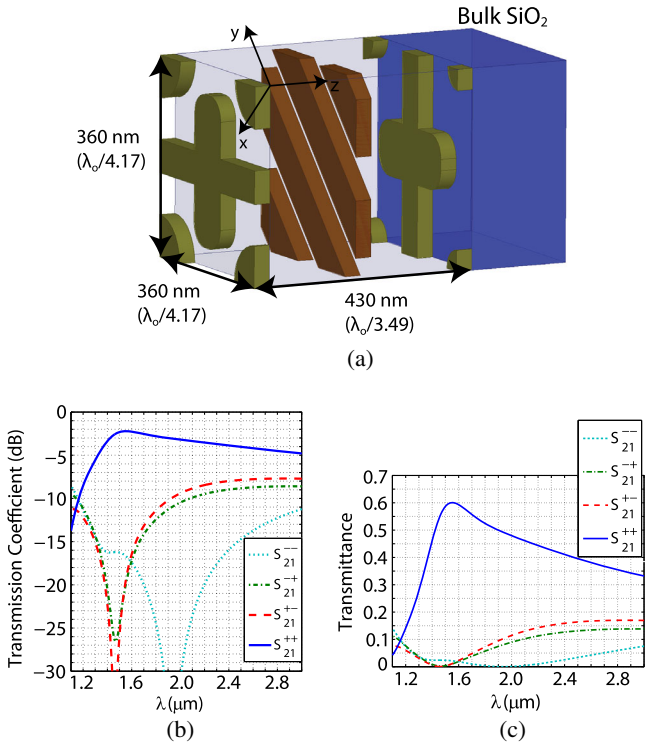

FIG. 7. Symmetric circular polarizer at near-infrared wavelengths. The surface is designed to operate at a wavelength of 1.5 μm. (a) Schematic of the unit cell. (b) Transmission coefficient, where the superscript + denotes right-handed circular and − denotes left-handed circular. (c) Transmittance ($|\mathbf{S}_{21}|^2$) on a linear scale.

V. SUMMARY

Closed-form expressions are derived that relate the reflection and transmission coefficients of a general bianisotropic metasurface to its constituent surface parameters. In addition, a systematic method to design bianisotropic metasurfaces is reported. Specifically, it is analytically shown that cascading anisotropic, patterned metallic sheets provide control of the electric, magnetic, and magnetoelectric coupling responses. This geometry is particularly attractive, because it allows for straightforward design and fabrication from microwave to optical wavelengths. Four different polarization-controlling devices are reported, each of which exhibits significantly improved performance over the state of the art.

Only homogeneous metasurfaces are considered here. In the future, a bianisotropic response could be added to inhomogeneous metasurfaces that simultaneously control both the polarization and phase of a wave front [57]. If lossy materials are used, this work can find applications in perfect absorbers [58]. In addition, this work could enable the development of polarimetric and spectroscopic

techniques for physics and chemistry [9,37]. Further, three-dimensional metamaterials can also benefit from this work [38]. By cascading the unit cell in the propagation direction ($\hat{z}$ direction), a bulk bianisotropic response is attainable [59].

ACKNOWLEDGMENTS

The authors acknowledge helpful discussions with Dr. Nicholaos Limberopoulos and Dr. Boris Tomasic from the Sensors Directorate, Air Force Research Laboratory. This work is supported by the Air Force Research Laboratory through the Advanced Materials, Manufacturing and Testing Information Analysis Center (AMMTIAC) contract with Alion Science and Technology, Contract No. FA4600-060D003, the National Science Foundation Materials Research Science and Engineering Center program DMR 1120923 (Center for Photonics and Multiscale Nanomaterials at the University of Michigan), and a Presidential Early Career Award for Scientists and Engineers No. FA9550-09-1-0696.

[1] N. Yu and F. Capasso, Flat optics with designer metasurfaces, Nat. Mater. **13**, 139 (2014).
[2] A. V. Kildishev, A. Boltasseva, and V. M. Shalaev, Planar photonics with metasurfaces, Science **339**, 1232009 (2013).
[3] A. Silva, F. Monticone, G. Castaldi, V. Galdi, A. Alù, and N. Engheta, Performing mathematical operations with metamaterials, Science **343**, 160 (2014).
[4] A. Grbic, L. Jiang, and R. Merlin, Near-field plates: Subdiffraction focusing with patterned surfaces, Science **320**, 511 (2008).
[5] N. Yu, P. Genevet, M. A. Kats, F. Aieta, J. P. Tetienne, F. Capasso, and Z. Gaburro, Light propagation with phase discontinuities: Generalized laws of reflection and refraction, Science **334**, 333 (2011).
[6] C. Pfeiffer and A. Grbic, Metamaterial huygens' surfaces: Tailoring wave fronts with reflectionless sheets, Phys. Rev. Lett. **110**, 197401 (2013).
[7] Michael Selvanayagam and George V. Eleftheriades, Discontinuous electromagnetic fields using orthogonal electric and magnetic currents for wavefront manipulation, Opt. Express **21**, 14409 (2013).
[8] F. Monticone, N. M. Estakhri, and A. Alù, Full control of nanoscale optical transmission with a composite metascreen, Phys. Rev. Lett. **110**, 203903 (2013).
[9] V. A. Fedotov, P. L. Mladyonov, S. L. Prosvirnin, A. V. Rogacheva, Y. Chen, and N. I. Zheludev, Asymmetric propagation of electromagnetic waves through a planar chiral structure, Phys. Rev. Lett. **97**, 167401 (2006).
[10] L. Wu, Z. Yang, Y. Cheng, M. Zhao, R. Gong, Y. Zheng, J. Duan, and X. Yuan, Giant asymmetric transmission of circular polarization in layer-by-layer chiral metamaterials, Appl. Phys. Lett. **103**, 021903 (2013).
[11] A. B. Khanikaev, S. H. Mousavi, G. Shvets, and Y. S. Kivshar, One-way extraordinary optical transmission and nonreciprocal spoof plasmons, Phys. Rev. Lett. **105**, 126804 (2010).
[12] Younes Ra'di, V. S. Asadchy, and S. A. Tretyakov, One-way transparent sheets, Phys. Rev. B **89**, 075109 (2014).
[13] T. Niemi, A. Karilainen, and S. Tretyakov, Synthesis of polarization transformers, IEEE Trans. Antennas Propag. **61**, 3102 (2013).
[14] Y. Ye and S. He, 90° polarization rotator using a bilayered chiral metamaterial with giant optical activity, Appl. Phys. Lett. **96**, 203501 (2010).
[15] C. Menzel, C. Rockstuhl, and F. Lederer, Advanced Jones calculus for the classification of periodic metamaterials, Phys. Rev. A **82**, 053811 (2010).
[16] S. Zhang, F. Liu, T. Zentgraf, and J. Li, Interference-induced asymmetric transmission through a monolayer of anisotropic chiral metamolecules, Phys. Rev. A **88**, 023823 (2013).
[17] A. Shaltout, V. Shalaev, and A. Kildishev, Homogenization of bi-anisotropic metasurfaces, Opt. Express **21**, 21941 (2013).
[18] Tianhua Feng, Fu Liu, Wing Yim Tam, and Jensen Li, Effective parameters retrieval for complex metamaterials with low symmetries, Europhys. Lett. **102**, 18003 (2013).
[19] C. L. Holloway, E. F. Kuester, and A. Dienstfrey, Characterizing metasurfaces/metafilms: The connection between surface susceptibilities and effective material properties, IEEE Antennas Wireless Propag. Lett. **10**, 1507 (2011).
[20] E. F. Kuester, M. A. Mohamed, M. Piket-May, and C. L. Holloway, Averaged transition conditions for electromagnetic fields at a metafilm, IEEE Trans. Antennas Propag. **51**, 2641 (2003).
[21] C. L. Holloway, E. F. Kuester, J. A. Gordon, J. O'Hara, J. Booth, and D. R. Smith, An overview of the theory and applications of metasurfaces: The two-dimensional equivalents of metamaterials, IEEE Antennas Propag. Mag. **54**, 10 (2012).
[22] J. A. Kong, Theorems of bianisotropic media, Proc. IEEE **60**, 1036 (1972).
[23] See Supplemental Material at http://link.aps.org/supplemental/10.1103/PhysRevApplied.2.044011 for additional details on the measurement procedures, exact dimensions, simulations, and analyses.
[24] D. R. Smith, S. Schultz, P. Markoš, and C. M. Soukoulis, Determination of effective permittivity and permeability of metamaterials from reflection and transmission coefficients, Phys. Rev. B **65**, 195104 (2002).
[25] M. A. Al-Joumayly and N. Behdad, Wideband planar microwave lenses using sub-wavelength spatial phase shifters, IEEE Trans. Antennas Propag. **59**, 4542 (2011).
[26] Y. Zhao, N. Engheta, and A. Alù, Homogenization of plasmonic metasurfaces modeled as transmission-line loads, Metamaterials **5**, 90 (2011).
[27] Carl Pfeiffer, Naresh Kumar Emani, Amr M. Shaltout, Alexandra Boltasseva, Vladimir M. Shalaev, and Anthony Grbic, Efficient light bending with isotropic metamaterial huygens' surfaces, Nano Lett. (to be published).
[28] N. Liu, H. Guo, L. Fu, S. Kaiser, H. Schweizer, and H. Giessen, Three-dimensional photonic metamaterials at optical frequencies, Nat. Mater. **7**, 31 (2008).
[29] Carl Pfeiffer, Cheng Zhang, Vishva Ray, L. J. Guo, and Anthony Grbic, High performance bianisotropic

metasurfaces: Asymmetric transmission of light, Phys. Rev. Lett. **113**, 023902 (2014).
[30] C. Pfeiffer and A. Grbic, Cascaded metasurfaces for complete phase and polarization control, Appl. Phys. Lett. **102**, 231116 (2013).
[31] C. Pfeiffer and A. Grbic, Millimeter-wave transmitarrays for wavefront and polarization control, IEEE Trans. Microwave Theory Tech. **61**, 4407 (2013).
[32] Y. Zhao, M. A. Belkin, and A. Alù, Twisted optical metamaterials for planarized ultrathin broadband circular polarizers, Nat. Commun. **3**, 870 (2012).
[33] B. A. Munk, *Frequency Selective Surfaces: Theory and Design* (Wiley, New York, 2005).
[34] J. Ma, R. Mittra, and N. T. Huang, Analysis of multiple fss screens of unequal periodicity using an efficient cascading technique, IEEE Trans. Antennas Propag. **53**, 1401 (2005).
[35] Chihhui Wu, Nihal Arju, Glen Kelp, Jonathan A Fan, Jason Dominguez, Edward Gonzales, Emanuel Tutuc, Igal Brener, and Gennady Shvets, Spectrally selective chiral silicon metasurfaces based on infrared Fano resonances, Nat. Commun. **5**, 3892 (2014).
[36] J. E. Roy and L. Shafai, Reciprocal circular-polarization-selective surface, IEEE Antennas Propag. Mag. **38**, 18 (1996).
[37] A. V. Rogacheva, V. A. Fedotov, A. S. Schwanecke, and N. I. Zheludev, Giant gyrotropy due to electromagnetic-field coupling in a bilayered chiral structure, Phys. Rev. Lett. **97**, 177401 (2006).
[38] J. B. Pendry, A chiral route to negative refraction, Science **306**, 1353 (2004).
[39] P. F. Goldsmith, Quasi-optical techniques, Proc. IEEE **80**, 1729 (1992).
[40] S. Gregson, J. McCormick, and C. Parini, *Principles of Planar Near-Field Antenna Measurements* (Institution of Engineering and Technology, London, 2007), Vol. 53.
[41] A. Yaghjian, An overview of near-field antenna measurements, IEEE Trans. Antennas Propag. **34**, 30 (1986).
[42] J. Wells, Faster than fiber: The future of multi-g/s wireless, IEEE Microw. Mag. **10**, 104 (2009).
[43] M. Schneider, in *Proceedings of the 2005 German Microwave Conference (GeMiC 2005)* (University of Ulm, Ulm, Germany, 2005), pp. 144–147.
[44] C. Menzel, C. Helgert, C. Rockstuhl, E. B. Kley, A. Tünnermann, T. Pertsch, and F. Lederer, Asymmetric transmission of linearly polarized light at optical metamaterials, Phys. Rev. Lett. **104**, 253902 (2010).
[45] M. Mutlu, A. E. Akosman, A. E. Serebryannikov, and E. Ozbay, Diodelike asymmetric transmission of linearly polarized waves using magnetoelectric coupling and electromagnetic wave tunneling, Phys. Rev. Lett. **108**, 213905 (2012).
[46] Ci Huang, Yijun Feng, Junming Zhao, Zhengbin Wang, and Tian Jiang, Asymmetric electromagnetic wave transmission of linear polarization via polarization conversion through chiral metamaterial structures, Phys. Rev. B **85**, 195131 (2012).
[47] N. K. Grady, J. E. Heyes, D. R. Chowdhury, Y. Zeng, M. T. Reiten, A. K. Azad, A. J. Taylor, D. A. R. Dalvit, and H. Chen, Terahertz metamaterials for linear polarization conversion and anomalous refraction, Science **340**, 1304 (2013).
[48] Z. Y. Yang, M. Zhao, P. X. Lu, and Y. F. Lu, Ultrabroadband optical circular polarizers consisting of double-helical nanowire structures, Opt. Lett. **35**, 2588 (2010).
[49] J. K. Gansel, M. Thiel, M. S. Rill, M. Decker, K. Bade, V. Saile, G. von Freymann, S. Linden, and M. Wegener, Gold helix photonic metamaterial as broadband circular polarizer, Science **325**, 1513 (2009).
[50] P. B. Johnson and R. Christy, Optical constants of the noble metals, Phys. Rev. B **6**, 4370 (1972).
[51] K. Chen, V. P. Drachev, J. D. Borneman, A. V. Kildishev, and V. M. Shalaev, Drude relaxation rate in grained gold nanoantennas, Nano Lett. **10**, 916 (2010).
[52] I. Tarn and S. Chung, A new advance in circular polarization selective surface—A three layered cpss without vertical conductive segments, IEEE Trans. Antennas Propag. **55**, 460 (2007).
[53] R. Pierrot, French Republic Patent 89.609, No. 1.512.598 (30 December 1966).
[54] G. A. Morin, in *Proceedings of the IEEE Antennas and Propagation Society International Symposium* (IEEE, New York, 1990), pp. 100–103.
[55] W. V. Tilston, T. Tralman, and S. M. Khanna, in *Proceedings of the IEEE Antennas and Propagation Society International Symposium* (IEEE, New York, 1988), pp. 762–765.
[56] Y. Ye, X. Li, F. Zhuang, and S. Chang, Homogeneous circular polarizers using a bilayered chiral metamaterial, Appl. Phys. Lett. **99**, 031111 (2011).
[57] Carl Pfeiffer and Anthony Grbic, Controlling vector Bessel beams with metasurfaces, following paper, Phys. Rev. Applied **2**, 044012 (2014).
[58] A. Serdyukov, I. Semchenko, S. Tretyakov, and A. Sihvola, *Electromagnetics of Bi-anisotropic Materials: Theory and Applications* (Gordon and Breach, Amsterdam, 2001).
[59] C. Fietz and G. Shvets, Homogenization theory for simple metamaterials modeled as one-dimensional arrays of thin polarizable sheets, Phys. Rev. B **82**, 205128 (2010).